Photoacoustic field calculation for nonspherical axisymmetric fluid particles

2017 Biomed. Phys. Eng. Express 3 015017

(http://iopscience.iop.org/2057-1976/3/1/015017)

Biomedical Physics & Engineering Express

PAPER

Photoacoustic field calculation for nonspherical axisymmetric fluid particles

RECEIVED
27 July 2016

REVISED
19 December 2016

ACCEPTED FOR PUBLICATION
22 December 2016

PUBLISHED
30 January 2017

Ratan K Saha[1], **Subhajit Karmakar**[2], **Arunabha Adhikari**[3] **and Michael C Kolios**[4,5]

[1] Department of Applied Sciences, Indian Institute of Information Technology Allahabad, Jhalwa, Allahabad, 211012, India
[2] University Science Instrumentation Centre, The University of Burdwan, Bardhaman, 713104, India
[3] Department of Physics, West Bengal State University, Berunanpukuria, North 24 Parganas, 700126, India
[4] Department of Physics, Ryerson University, 350 Victoria Street, Toronto, ON, M5B 2K3, Canada
[5] Institute for Biomedical Engineering, Science and Technology (iBEST), a partnership between Ryerson University and St. Michaels Hospital, 209 Victoria Street, Toronto, Ontario, M5B 1T8, Canada

E-mail: ratank.saha@iiita.ac.in

Keywords: Green's function, spheroids, erythrocyte, stomatocyte, Chebyshev particles, Legendre polynomial

Abstract

The photoacoustic (PA) field calculation using a Green's function approach for nonspherical axisymmetric fluid particles is discussed. The PA fields have been computed for spheroidal droplets, Chebyshev particles and normal and pathological red blood cells (RBCs) over a large frequency band (10–1000 MHz). Theoretically constructed RBC contours have been fitted using the Legendre polynomial expansion for parametrization of cell shapes. It is shown that first minimum of the PA spectrum appears at a lower frequency as the width of the particle along the direction of measurement increases. The spectra for higher order ($n = 6, 8$) Chebyshev particles resembled that of an equivalent sphere up to first minimum. The first minimum for a stomatocyte appeared (420 MHz) much earlier compared to that (640 MHz) of normal RBC when measured along the direction of the symmetry axis; whereas the locations were 310 and 240 MHz, respectively from a perpendicular direction. The evaluation of cellular morphology might be feasible by analyzing the single particle PA spectrum.

1. Introduction

Several methods have been developed to study light scattering by a variety of particles, namely, particulate matter, biological cells and tissues. The Mie theory, which is an exact method, has been extensively employed to obtain scattering solutions for regular (e.g. spherical, cylindrical etc) objects [1]. Waterman developed a method known as the *T*-matrix method to examine light scattering by nonspherical particles [2, 3]. This approach has found important applications in many fields such as characterization of optical properties of aerosol particles [1]. Another approach referred to as the discrete dipole approximation has been developed as a flexible and powerful technique for computing scattering and absorption by targets of arbitrary geometry [4]. The Born approximation method has been used to yield scattering solutions for soft particles [5]. In the context of ultrasonic scattering, scattering solutions for solid regular targets can be obtained using the Faran model [6]. The angular distribution of scattering amplitude for fluid spheres can be calculated analytically too [7]. Waterman's *T*-matrix formulation has also been implemented to investige acoustic scattering of erythrocyte suspension [8, 9]. There also exist some approximate methods based on the Born approximation and its variants yielding scattering solutions for weak scatterers [10]. In these cases, the wave equation is solved using a Green's function method.

The exact analytical solutions to the photoacoustic (PA) wave equation can be derived using separation of variables method for sources with regular shapes [11]. The exact solution for a fluid sphere can faithfully model PA fields generated by fluid droplets [11]. It has also been used to represent PA signals from cells [12–17]. If the single particle solution is known, the resultant PA field generated by many particles (or a tissue) can be obtainted by linearly summing fields emitted by the individual cells. This is the approach adopted to study how time and spectral domain features of PA signals are dependent on the spatial organization or size distribution of cells [12, 14, 16, 17]. The same single particle theoretical formulation has been applied to

investigate how biophysical and biochemical properties of cells affect PA signal properties [13–17]. An inverse problem framework has been recently proposed to assess mean size and average variance in the optical absorption coefficients of tissue microstructures from received PA signals [18]. It analyzes PA signals in the frequency domain using correlation models. It may be noted that in these studies cells are assumed as fluid spheres which seems to be a valid approximation, at least in the low frequency range [19, 20].

Strohm *et al*, in fact, experimentally demonstrated that spherical approximation is not valid above 100 MHz for PA sources like red blood cells (RBCs) [19, 20]. The PA signals from a series of normal and treated RBCs were measured at different orientations using ultra-high frequency transducers (with center frequencies at 200, 375, 1200 MHz). They also performed numerical simulations using the finite element method to compare theoretical and experimental results. These works revealed that a micron-sized particle has unique spectral features above 100 MHz that are strongly dependent on size, shape and orientation of the particle. It is believed that these features could be exploited to help diagnose RBC pathology from just a single drop of blood in a clinical setting through an automated process. Recently, Li *et al* developed methods for calculating PA fields from spheroidal droplets [21, 22]. However, analytical derivation in a spheroidal coordinate system is nontrivial. On the other hand PA signal emitted by a source with arbitrary shape can be simulated using k-Wave tool box and accordingly, signal characteristics can be examined [23]. For example, this tool box has recently been explored to simulate PA waves for nanoparticles of various shapes [24]. However, in general, solution to the PA wave equation in 3D are resource intensive and time consuming. Therefore, a more efficient method to calculate the PA fields is desirable.

In this paper, we used a Green's function approach to solve the PA wave equation. It is a simple and fast procedure for obtaining solutions for regular and irregular objects. The detailed derivation of differential PA cross-section is also presented in this work. It is defined as the acoustic power received per unit solid angle divided by the intensity of the light beam. It has been developed by drawing analogy with light and sound scattering problems. The differential scattering cross-section can relate theoretical results with experimental findings. The total PA cross-section can be computed by integrating the differential PA cross-section over the whole solid angle. It can be thought as a hypothetical area for which light energy is converted into sound energy. Using this approach, we computed PA fields from nonspherical axisymmetric fluid particles, including spheroidal droplets, the Chebyshev particles [26] and normal and pathological RBCs. The first two classes of particles are theoretically interesting to study whereas the third set of corpuscles have been investigated to gain insights for developing a PA characterization tool to assess cellular morphology. Parametric surface modeling approach involving the Legendre polynomial expansion has been implemented to construct contours of discocyte and stomatocyte states of RBCs. It is shown that locations of spectral minima depend upon the size of particles and direction of measurement. The numerical results presented in this paper were validated by performing 2D simulations using the k-Wave simulation tool box [23].

The organization of the paper is as follows. Section 2 presents the mathematical derivation for calculating the differential PA cross-section. The parametric descriptions of various shapes and numerical parameters are also given in this section. The next section describes the numerical results. A discussion of the merits of the current approach is presented in section 4. The conclusions of this study are drawn in the same section as well.

2. Materials and methods

2.1. PA field calculation

The time independent wave equation for PA pressure is given by,

$$\nabla^2 p + k^2 p = \begin{cases} \frac{\mathrm{i}\omega\mu\beta I_0}{C_P}, & \text{inside the absorber} \\ 0, & \text{outside the absorber,} \end{cases} \quad (1)$$

where μ, β, C_P are the optical absorption coefficient, isobaric thermal expansion coefficient and specific heat for the absorbing region, respectively. Here, ω and I_0 indicate modulation frequency and intensity of the incident light beam; k is the wave number of the acoustic wave. The acoustic properties (e.g. density and speed of sound) of the absorbing and the ambient media are similar. The solution to equation (1) can be obtained as [25],

$$p_{\mathrm{ext}}(\mathbf{r}, k) = -\int A\, G(\mathbf{r}|\mathbf{r}_0)\, \mathrm{d}^3\mathbf{r}_0, \quad (2)$$

where $A = \frac{\mathrm{i}\mu\beta I_0\omega}{C_P}$; $G(\mathbf{r}|\mathbf{r}_0)$ is the free space Green's function; $\mathbf{r}(r, \theta, \phi)$ and $\mathbf{r}_0(r_0, \theta_0, \phi_0)$ denote field and source points, respectively as shown in figure 1. The subscript ext indicates that the field point is outside the absorbing region (i.e. $r > r_0$). The free space Green's function is given by [25],

$$G(\mathbf{r}|\mathbf{r}_0) = \frac{\mathrm{e}^{\mathrm{i}k|\mathbf{r}-\mathbf{r}_0|}}{4\pi|\mathbf{r} - \mathbf{r}_0|}. \quad (3)$$

In the far field ($r \gg r_0$), Green's function can be approximated as $G(\mathbf{r}|\mathbf{r}_0) \approx (1/4\pi r)\mathrm{e}^{\mathrm{i}kr}\mathrm{e}^{-\mathrm{i}\mathbf{k}\cdot\mathbf{r}_0}$ with $\mathbf{k}$ as the direction of measurment and thus equation (2) becomes,

$$p_{\mathrm{ext}}(\mathbf{r}, k) \approx -\frac{\mathrm{e}^{\mathrm{i}kr}}{4\pi r}\int A\, \mathrm{e}^{-\mathrm{i}\mathbf{k}\cdot\mathbf{r}_0}\mathrm{d}^3\mathbf{r}_0 = \frac{\mathrm{e}^{\mathrm{i}kr}}{r}M(\mathbf{k}), \quad (4)$$

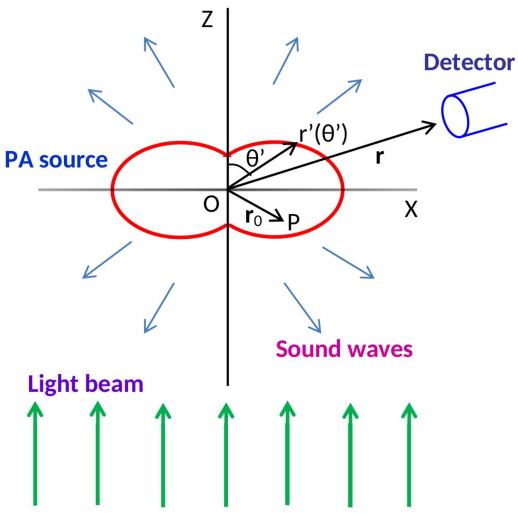

Figure 1. Geometry of the PA set up.

where

$$M(\mathbf{k}) = -\frac{1}{4\pi}\int A\, e^{-i\mathbf{k}\cdot\mathbf{r}_0} d^3\mathbf{r}_0. \quad (5)$$

Analogous to the differential scattering cross-section, differential PA cross-section (defined as the acoustic power per unit solid angle received far away from the PA source divided by the intensity of the light beam) can be expressed as [18],

$$\sigma(k) = \frac{|M(\mathbf{k})|^2}{2\rho v I_0}, \quad (6)$$

where ρ and v are the density and speed of sound of the surrounding medium. Scattering cross-sections have been computed and measured in various branches of science to study scattering properties of imhomogeneities. The total PA cross-section can readily be calculated by integrating the differential PA cross-section $\sigma(k)$ over the entire solid angle. The total PA cross-section indicates a hypothetical area and light energy of which converts into acoustic energy due to the PA effect. For a regular object, integration in equation (5) can be calculated analytically providing a closed form expression for $\sigma(k)$. For example, for a homogeneous spherical absorber equation (6) reduces to,

$$\sigma(k) = \frac{\mu^2\beta^2 I_0 v}{2\rho C_P^2}\varrho^4 [j_1(k\varrho)]^2, \quad (7)$$

where j_1 is the spherical Bessel function of order unity and ϱ is the radius of the spherical absorber. For an irregular PA source, it is not possible to yield analytical solution, however, a numerical solution can be obtained.

The time domain form for PA pressure for a delta function heating pulse can be written as [11],

$$p_{ext}(\mathbf{r}, t) \approx \frac{i\mu\beta F}{2\pi C_P}\int_{-\infty}^{\infty} d\omega\, \omega\, e^{-i\omega t} \times \left[-\frac{e^{ikr}}{4\pi r}\int e^{-i\mathbf{k}\cdot\mathbf{r}_0} d^3\mathbf{r}_0\right], \quad (8)$$

where F is the optical fluence. It may be emphasized here that equation (8) represents an analytic signal. Thus, the real and the imaginary parts form a Hilbert transform pair. The real part has been considered as the PA signal. In this work, equation (8) has been numerically evaluated to simulate PA signals for some of the shapes considered in this study.

2.2. Axisymmetric nonspherical shapes

2.2.1. Spheroidal droplets

The geometry of an irregular absorber having azimuthal symmetry can be described in spherical polar coordinates (r', θ', ϕ') by setting, $r' = F(\theta')$; F is a function that relates r' and θ' (see figure 1). For example, for a spheroidal particle we can write the distance $r'(\theta')$ of a point on the surface to be,

$$r'(\theta') = \frac{ab}{[b^2\sin^2\theta' + a^2\cos^2\theta']^{1/2}}, \quad (9)$$

where a and b are the semi axes (for oblate sphere $b < a$ and for prolate sphere $b > a$). Figure 2 shows some spheroids with different aspect ratios that have been considered in this study. For all droplets the volume remains the same. Equations (2) and (5) for a nonspherical object can be simplified as,

$$p_{ext}(\mathbf{r}, k) = -\frac{e^{ikr}}{4\pi r}A\int_0^{\pi}\sin\theta_0 d\theta_0\int_0^{F(\theta_0)} r_0^2 dr_0 \times \int_0^{2\pi} e^{-i\mathbf{k}\cdot\mathbf{r}_0} d\phi_0, \quad (10)$$

$$M(\mathbf{k}) = -\frac{A}{4\pi}\int_0^{\pi}\sin\theta_0 d\theta_0\int_0^{F(\theta_0)} \times r_0^2 dr_0\int_0^{2\pi} e^{-i\mathbf{k}\cdot\mathbf{r}_0} d\phi_0, \quad (11)$$

respectively. The above integration was numerically calculated in this work to generate PA fields and accordingly differential PA cross-sections for various spherical and axisymmetric nonspherical light absorbing particles.

2.2.2. Chebyshev particles

For a Chebyshev particle, distance of a point on the surface can be written as [26],

$$r'(\theta') = R_c[1 + \epsilon T_n(\cos\theta')], \quad (12)$$

where $T_n(\cos\theta') = \cos n\theta'$ is the Chebyshev polynomial of degree n, n refers to the waviness parameter, R_c is the radius of the unperturbed sphere and ϵ is the deformation parameter. Such a particle is obtained by continuously deforming a sphere using a Chebyshev polynomial of degree n. Scattering properties of this two parameter family of particles have been studied extensively in the field of light scattering [26]. Some of the Chebyshev particles at fixed volume are shown in

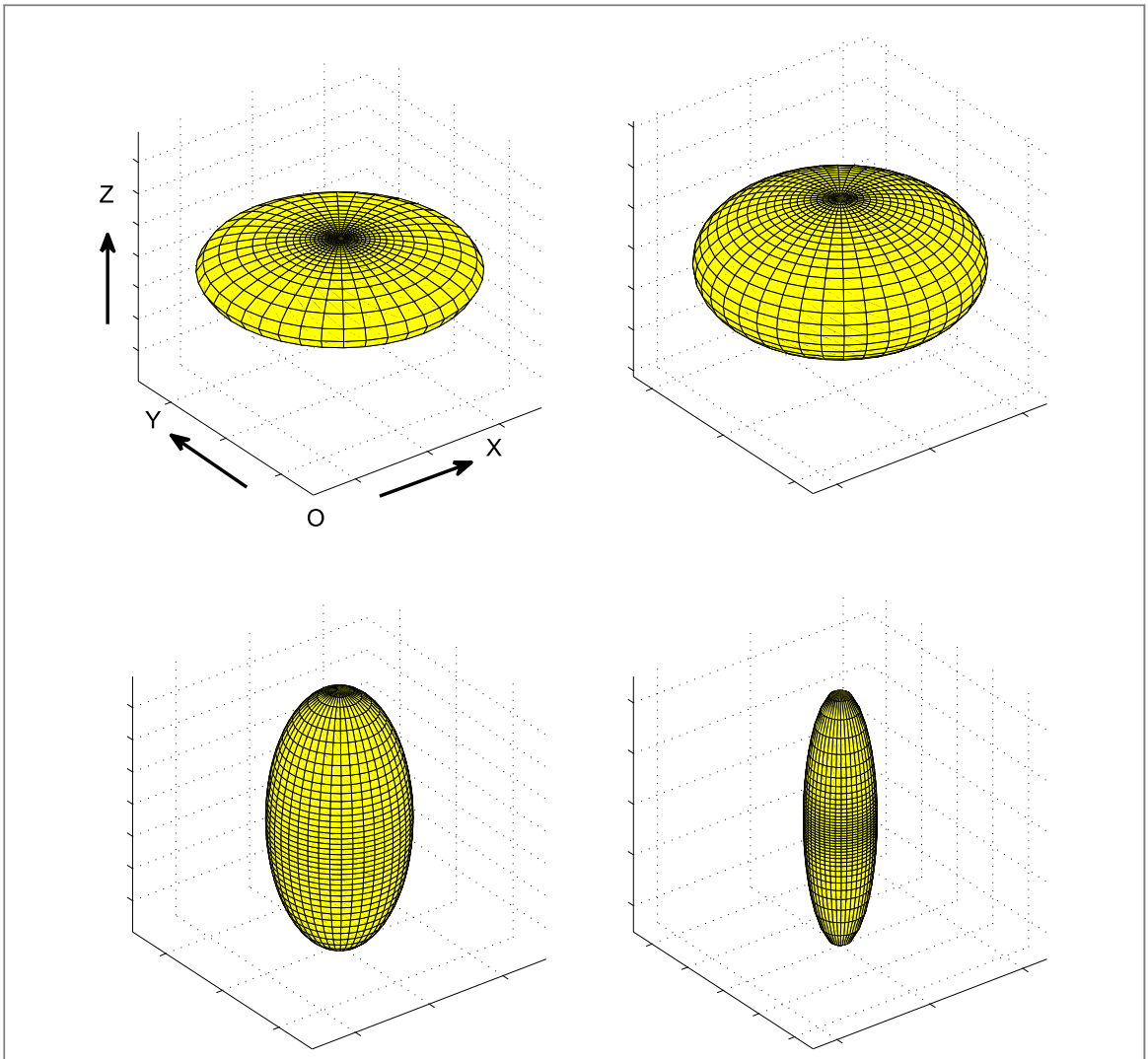

Figure 2. Representative plots of spheroidal droplets with constant volume; b:a = 1:4 (top row, left panel), b:a = 1:2 (top row, right panel), b:a = 2:1 (bottom row, left panel), b:a = 4:1 (bottom row, right panel).

figure 3 for $\epsilon = 0.25$ and figure 4 for $\epsilon = -0.25$. The particles are symmetric with respect to the Z axis (see figure 3(a)). The particles with even n are also symmetric with respect to a plane perpendicular to the symmetry axis. The particles with odd n are not symmetric about the same plane. The heights of peaks/troughs of dips (of surface curvature) increase as the magnitude of ϵ increases. However, the number of peaks and dips increases with increasing n. The frequency domain solution of PA field can be computed utilizing equation (11) for the Chebyshev particles.

2.2.3. Red blood corpuscles

RBCs under the normal physiological conditions appear as biconcave discocytes. It has been known for more than 50 years that there are many biochemical agents that can modify RBC morphology [27, 28]. Some agents can induce a series of crenated shapes known as echinocytes. For such cells, many little equally spaced protrusions are projected outwards. There are several agents that can induce concave shapes referred to as stomatocytes. Both normal and pathological shapes can be fitted well with spherical harmonics expansion [29, 30]. In fact, spherical harmonics expansion has been found to be a convenient tool to parametrize cell morphology. This set of functions can fit both symmetrical and nonsymmetrical objects. The fitting problem becomes relatively simple for azimuthally symmetric particles. In this case, cell contour can be expanded in terms of the Legendre polynomials as,

$$r'(\theta') = R_e\left[1 + \sum_n \alpha_n P_n(\cos\theta')\right], \qquad (13)$$

where R_e is the radius of spherical envelope that encloses RBC; α_n is the parameter describing the shape and P_n is the Legendre polynomial of degree n. It may be noted that the Legedre polynomials are orthogonal functions and form complete set of basis functions. Any arbitrary function between $0 \leqslant \theta' \leqslant \pi$ can be expressed in terms of these basis vectors. In this study, we use the above expansion to obtain normal discocyte shape and two different shapes simulating stomatocytes. The 2D cross-sectional views of the shapes are

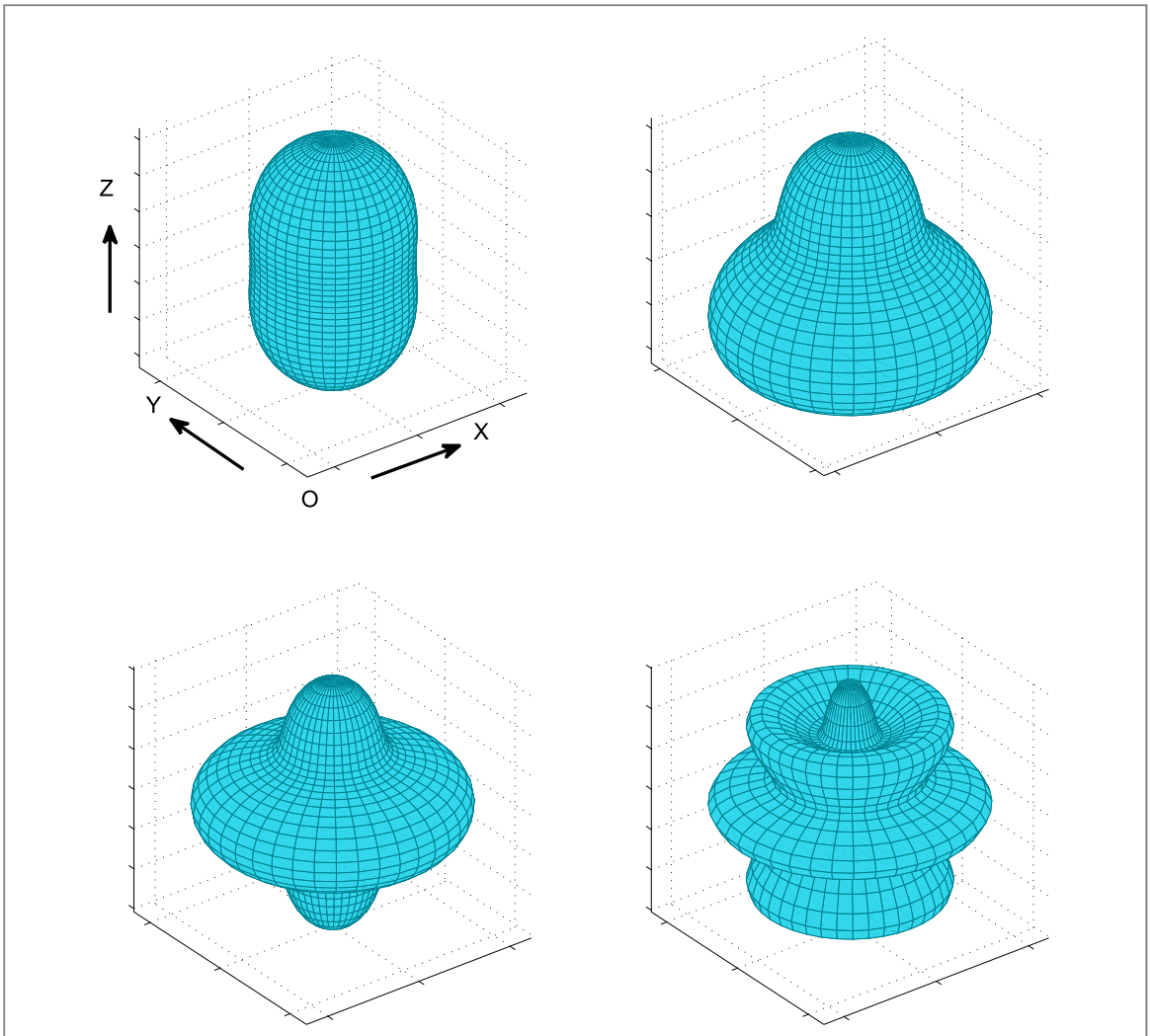

Figure 3. The Chebyshev particles with $\epsilon = 0.25$; $n = 2$ (top row, left panel), $n = 3$ (top row, right panel), $n = 4$ (bottom row, left panel) and $n = 8$ (bottom row, right panel).

given in figures 5(a)–(c) and 3D shapes in figure 6. The PA fields, as well as differential PA cross-sections, have been computed for those corpuscles.

2.3. Numerical parameters

2.3.1. Physical parameters

The density and speed of sound of the surrouding medium were chosen as $\rho = 1005\,\mathrm{kg\,m^{-3}}$ and $v = 1500\,\mathrm{m\,s^{-1}}$, respectively. The same values were also taken for the PA source. The optical and thermo-mechanical parameters for the absorbing object were taken as constants ($I_0 = 1$, $\mu = 1$, $\beta = 1$, $C_P = 1$). PA pressure amplitudes were evaluated for a wide range of frequencies from 1.5 to 2000 MHz. To carry out the integration in equation (11), the source volume was discritized into a number of voxels (200 nm as the length of each side). The trapezoidal rule was used to perform the numerical integrations. A computer code was written in MATLAB for this purpose. It was executed in a personal computer (Intel(R) Core(TM) i3-3220 CPU, 3.30 GHz, 6 GB RAM). Figure 7 shows a comparison between numerical and analytical results for a homogeneous spherical PA source (of 5 μm radius). Excellent match between these curves validates the numerical scheme implemented in this study.

2.3.2. Shape parameters

The differential PA cross-section was calculated for eight spheroidal shapes with aspect ratios b:a = 1:8, 1:4, 1:2, 2:1, 4:1, 8:1. The shape parameters are given in table 1. For the second case, we considered ten different Chebyshev shapes (see table 1 for parameter specification). For each case, volume was fixed at 523.6 $\mu\mathrm{m}^3$, which is the volume of a fluid sphere of radius 5 μm.

The parametric equation of the Evans–Fung model has been extensively used to generate contour of a healthy RBC and it is given by [31],

$$z(\xi) = R_e\sqrt{1-\left(\frac{\xi}{R_e}\right)^2}\left[c_0 + c_1\left(\frac{\xi}{R_e}\right)^2 + c_2\left(\frac{\xi}{R_e}\right)^4\right], \tag{14}$$

where ξ is the horizontal distance and three coefficients c_0, c_1 and c_2 determine RBC shape [3] (see figure 5). The numerical values of these coefficients

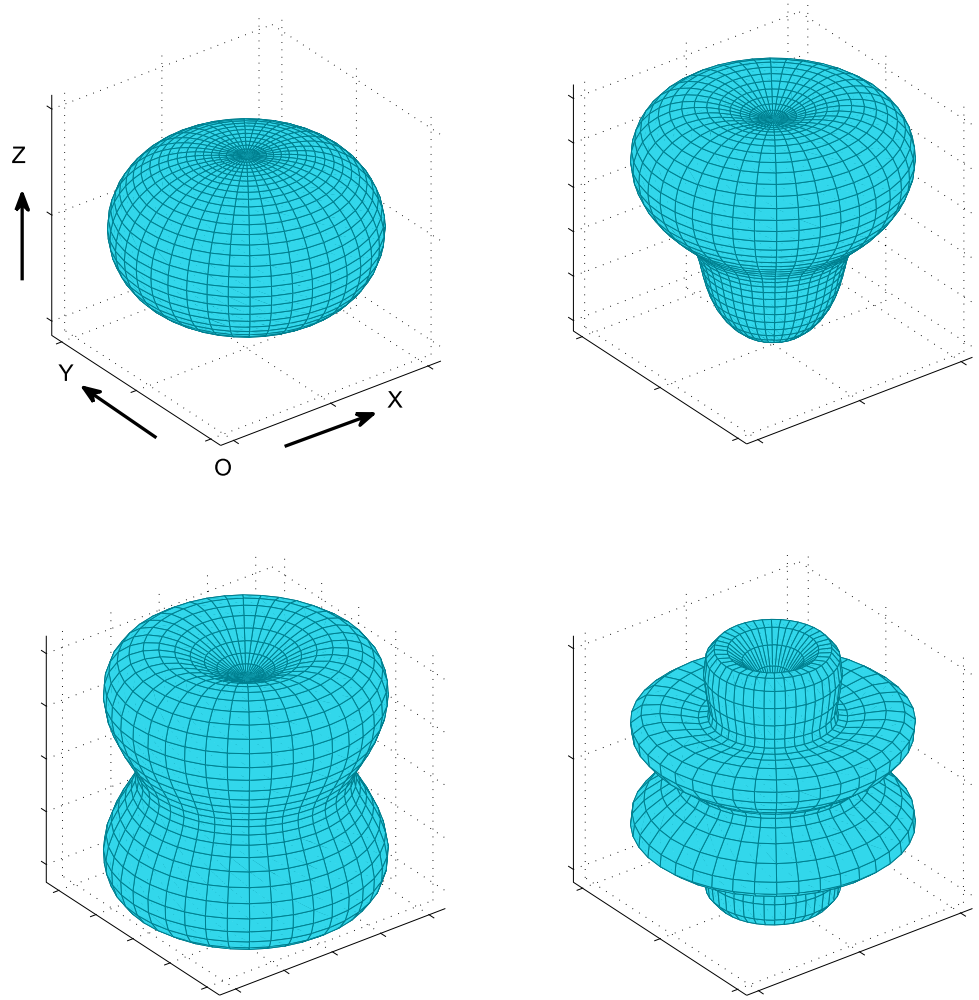

Figure 4. The Chebyshev particles with $\epsilon = -0.25$; $n = 2$ (top row, left panel), $n = 3$ (top row, right panel), $n = 4$ (bottom row, left panel) and $n = 8$ (bottom row, right panel).

can be obtained from four morphological parameters expected to be known from measurements. The morphological parameters, as shown in figures 5(a)–(c), are diameter (D), dimple thickness (t), maximum thickness (h), diameter of a circle drawn on the location of maximum thickness (d). The numerical values of these four morphological parameters for a normal RBC were taken from literature [3] and presented in table 1. Two shapes mimicking stomatocytes were simulated (referred to as Stomatocyte1 and Stomatocyte2 in the text) by varying these morphological parameters phenomenologically. For pathological RBCs, the upper hemisphere was generated using equation (14) while the lower part was a half sphere. 2D and 3D views of these cells are demonstrated in figures 5 and 6, respectively. The theoretically constructed shapes were then fitted with the expansion given in equation (13) in order to estimate α_n. At first we generated s number of radial samples (i.e. $r_1, r_2 ... r_s$) at different angular locations ($\theta_1, \theta_2 ... \theta_s$) using equation (14). Then we constructed a system of equations considering up to Lth degree Legendre polynomial as (see equation (13)),

$$\begin{pmatrix} P_0(\cos\theta_1) & P_1(\cos\theta_1) & .... & P_L(\cos\theta_1) \\ P_0(\cos\theta_2) & P_1(\cos\theta_2) & .... & P_L(\cos\theta_2) \\ \vdots & & & \\ P_0(\cos\theta_s) & P_1(\cos\theta_s) & .... & P_L(\cos\theta_s) \end{pmatrix} \times \begin{pmatrix} \alpha_0 \\ \alpha_1 \\ \vdots \\ \alpha_L \end{pmatrix} = \begin{pmatrix} r_1/R_e - 1 \\ r_2/R_e - 1 \\ \vdots \\ r_s/R_e - 1 \end{pmatrix}. \quad (15)$$

The above equations have been solved using the least square fitting technique obtaining α_n s. In this work, we generated more than 100 radial samples and infintie sum in equation (13) was truncated at $L = 19$, which was fixed based on the literature [30]. In fact, accuracy of fitting did not improve significantly if higher order terms were retained. The fitted curves are shown in figures 5(a)–(c) along with the theoretical curves (from equation (14)). Excellent agreement can be seen in figures 5(a)–(c). The relative strengths of α_n are plotted in figure 5(d) for each case. Reconstructed 3D shapes are displayed in figure 6.

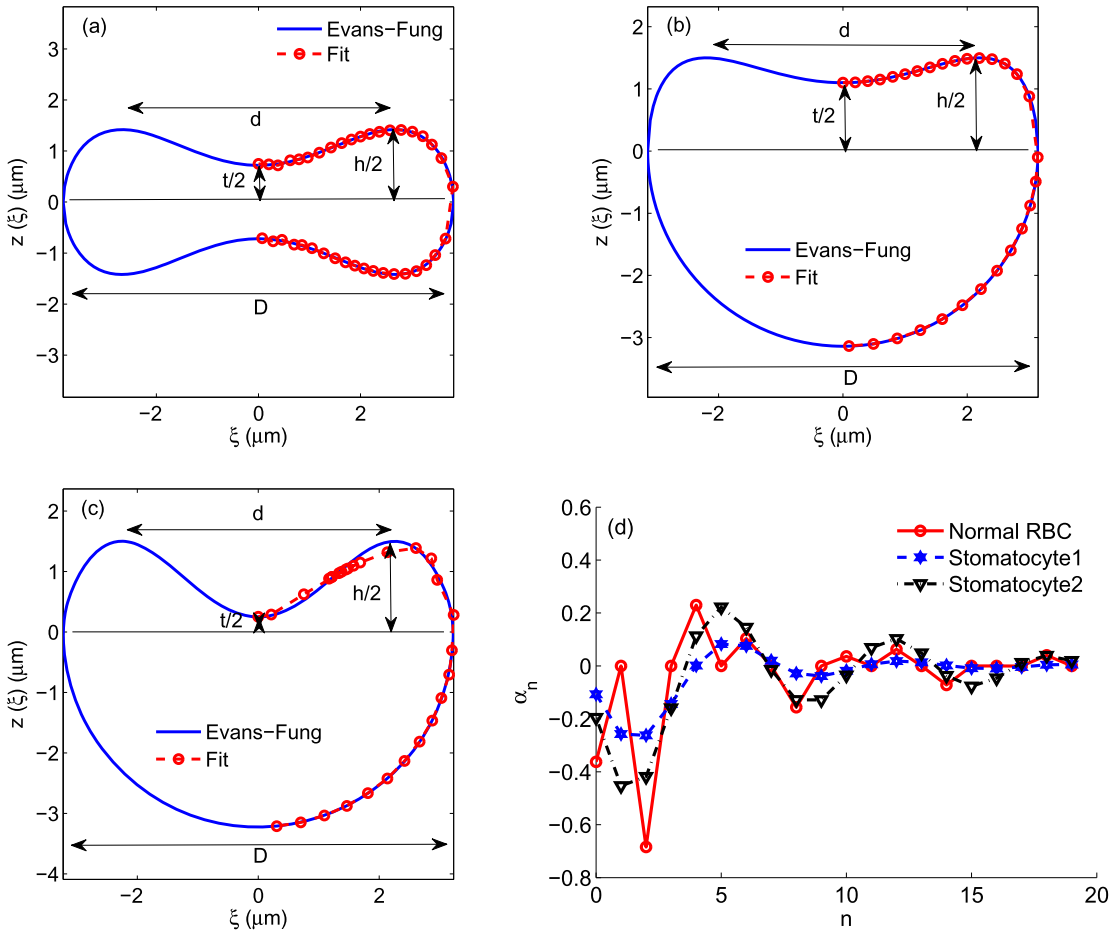

Figure 5. Two-dimensional cross-sections of normal and pathological RBCs. (a) Normal RBC, (b) Stomatocyte1, (c) Stomatocyte2. (d) Plots of coefficients (α_n) of the Legendre polynomials.

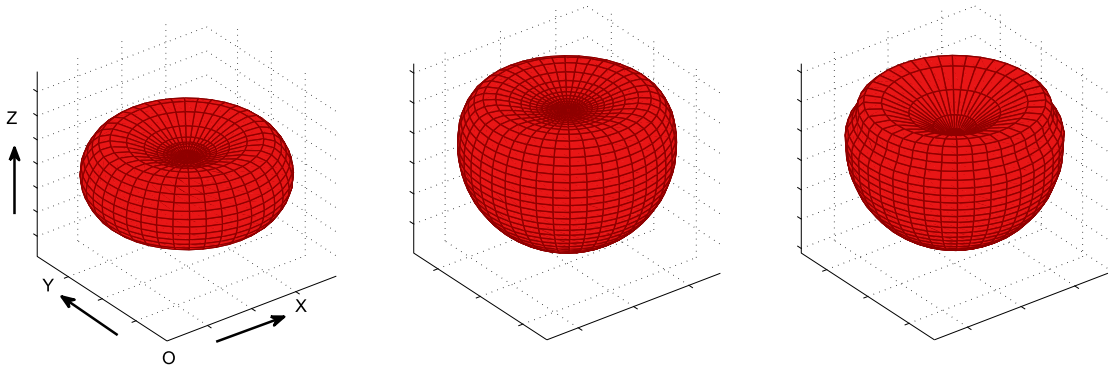

Figure 6. Simulated shapes of normal erythrocyte and stomatocytes. Left panel: normal RBC, middle panel: Stomatocyte1 and right panel: Stomatocyte2.

3. Results

Representative plots $|M(f)|^2$ for different oblate and prolate spheroids of the same volume are shown in figure 8(a) over a wide range of frequencies (10–1000 MHz). This quantity has been calculated along the axis of symmetry. The aspect ratio of each droplet is presented in the legend. To improve the clarity of the figure, lines are plotted in two subfigures and also some lines have been omitted. The result for an equivalent sphere (i.e. b:a = 1:1) is also included in the figure for comparison. Figure 8(a) shows that magnitudes of power spectra for different spheroidal objects are comparable at frequencies below 10 MHz. Shape variation does not affect spectral features in the low frequency range. After 10 MHz each curve passes through successive maxima and minima. The number of oscillations increases as the aspect ratio increases.

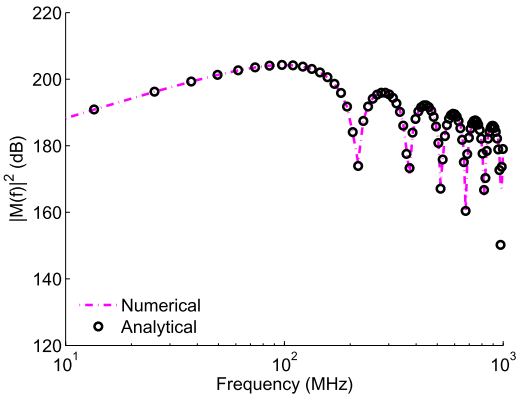

Figure 7. Comparison between analytical and numerical results for a homogeneous light absorbing sphere (of 5 μm radius).

Table 1. Numerical values of parameters for various PA sources. The unit for RBC morphological parameters is μm.

Objects	Volume (μm^3)	Shape parameters
Spheroids	523.6	b:a = 1:1
	523.6	b:a = 1:8, 1:4, 1:2, 2:1, 4:1, 8:1
Chebyshev	523.6	$\epsilon = 0$
	523.6	$\epsilon = 0.25, n = 2, 3, 4, 6, 8$
	523.6	$\epsilon = -0.25, n = 2, 3, 4, 6, 8$
RBCs	105.1	$D = 7.65, t/2 = 0.72, h/2 = 1.42,$ $R_e = 0.5D, d = 0.7D, L = 19$
	104.4	$D = 6.28, t/2 = 1.1, h/2 = 1.5,$ $R_e = 0.5D, d = 0.7D, L = 19$
	105	$D = 6.45, t/2 = 0.25, h/2 = 1.5,$ $R_e = 0.5D, d = 0.7D, L = 19$

The first minimum for the particle with b:a = 8:1 appears at the lowest frequency (approximately 50 MHz). In contrast, the spectrum for the object having b:a = 1:8 is nearly flat up to approximately 600 MHz. The first minimum for this particle arises at 860 MHz. The thickness of the particle along the direction of measurement controls the locations of first minimum as well as higher order spectral features (peaks and dips). The spectral maxima and minima for the intermediate particles occur at frequencies >100 MHz. Similar observations can be made from figure 8(b) which demonstrates power spectra for the same particles when measured perpendicular to the axis of symmetry. As expected, the curves are oriented in the reverse order with respect to figure 8(a).

Figure 9(a) illustrates how power spectra vary for a series of Chebyshev particles ($\epsilon = 0.25$; n = 2, 3, 6 and 8). This figure contains two parts (lower and upper panels) so that the graphs are displayed distinctly. The number of maxima and minima within 100–1000 MHz is maximum for $n = 2$. Additionally for this particle, oscillation starts earlier (first minimum at 150 MHz) compared to the others. This is due to the fact that it is the thickest particle, within this class of particles, along the axis of symmetry (see figure 3, top row, left panel). The spectrum for $n = 3$ has no spectral feature (flat) over the entire frequency range. The amplitude of oscillation of spectral features are noticeably smaller than those of the others. The first minima positions for $n = 6$ and 8 appear close to that of the sphere. Further, the gap between first and second minima for $n = 6$ or 8 is wider than that of two and three. The theoretical spectra for the same particles are demonstrated in figure 9(b) when computed in a transverse direction ($\theta = \pi/2$). The peak and trough pattern for $n = 2$ is similar to that of figure 9(a). However, minima locations because of lower thickness occur at higher frequencies in figure 9(b). The spectrum for $n = 3$ exhibits more pronounced spectral features (maxima and minima) at regular intervals in comparison to those of figure 9(a). The spectra for higher order particles resemble that of the sphere up to nearly 250 MHz. After that deviations are great owing to shape-complexity as compared to the PA wavelength. Figure 10 displays computed spectra for Chebyshev particles with $\epsilon = -0.25$ and n = 2, 3, 6 and 8. The spectra for $n = 2$ along $\theta = 0$ and $\pi/2$ manifest expected variations. The spectral signatures for $n = 3$ in figures 10(a) and (b) are identical with those of figures 9(a) and (b), respectively. As discussed above, spectra for complex shapes (i.e. $n = 6$ and 8) closely match with that of the sphere at least up to the first minimum. Thereafter spectral variations are complex and interpretation is not straight forward.

The spectral behaviors of normal and pathological RBCs are presented in figures 11(a) and (b) along and perpendicular to the symmetry axis, respectively. As mentioned earlier, two subfigures are used to plot the lines for each case for better presentation. The same curve for an equivalent sphere is also provided in both of the figures for comparison. The spectrum is flat and essentially featureless from 100 to 500 MHz for a healthy RBC as shown in figure 11(a). The first spectral minimum in this case appears at 640 MHz. An RBC is really thin along this direction (see figure 5(a)) and that pushes the first minimum to occur at a very high frequency. The spectra corresponding to stomatocyes are similar. The variation of thickness at the center is below 20% between the stomatocytes and thus seems to have negligible effect in the spectral domain. Nevertheless, the first minimum for stomatocytes appear much earlier (≈421 MHz), due to the change in shape of the cell, compared to that of normal erythrocyte. Several maxima and minima are enclosed within 100–500 MHz for biconcave RBC with the first minimum appearing at 241 MHz (figure 11(b)). The spectra for stomatocytes have feature patterns between those of normal and spherical RBCs since the diameters of the former particles (see figures 5(b) and (c)) lie between those of the later objects.

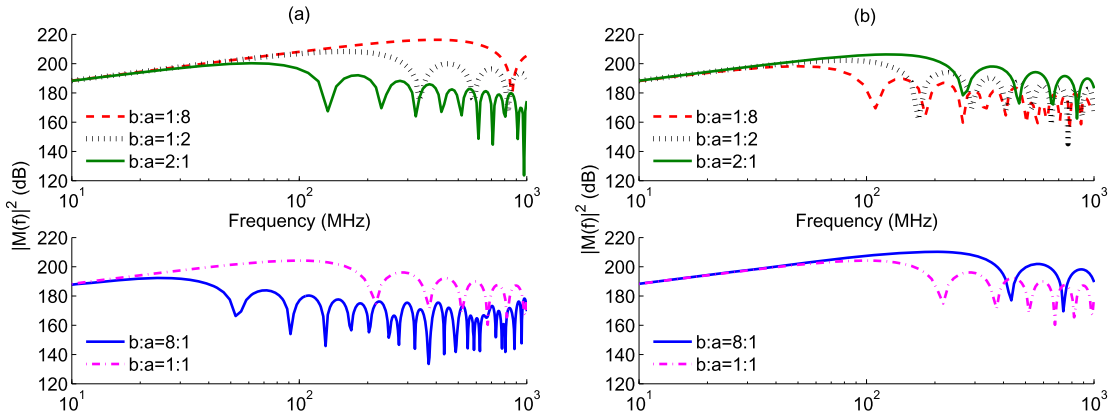

Figure 8. Plots of $|M(f)|^2$ as a function of frequency for different spheroids calculated along ($\theta = 0$) and perpendicular $\left(\theta = \frac{\pi}{2}\right)$ to the axis of symmetry in (a) and (b), respectively. To improve the clarity of each figure, lines are presented in two subfigures (upper and lower panels).

4. Discussion and conclusions

Various PA spectral lines generated by a series of particles at different orientations are presented in this work. These are obtained by direct computation of the frequency domain solution to the PA wave equation using a Green's function approach. It is demonstrated that spectral lines are different for different particles. Therefore, it is expected that the corresponding PA signals should be different for different particles too. To verify this, the PA signals from normal and pathological RBCs have been computed by numerically evaluating equation (8) and are displayed in figure 12. A sharp and narrow N-shaped pulse has been computed when the detector is located at $\theta = 0$ as shown in figure 12(a). The pulse is elongated when probed from $\theta = \pi/2$. Its amplitude is approximately reduced by a factor of four and the PA signal duration is three times greater than those of the former pulse. This can be attributed to the fact that RBC is thinner when viewed by the ultrasound detector from the first direction compared to the second direction. The difference between the PA signals emitted by Stomatocyte1 and Stomatocyte2 is small because they are similar (as given in figures 12(b) and (c)). As expected for a homogeneous sphere, signals are identical from all directions as shown in figure 12(d).

The spectral lines for the particles considered in this study were also generated via the k-Wave simulation tool box for comparison[6]. In this case, we performed simulations in 2D since 3D simulations in k-Wave are time consuming. Figure 13(a) displays the spectral lines for four RBC shapes (i.e. discocyte, Stomatocyte1, Stomatocyte2 and spherical) for the observation direction $\theta = 0°$. The graphs for the method presented in this work for the same 2D particles are shown in figure 13(b). The locations of frequency minima as well as spectral slope up to 200 MHz for each line in figure 13(a) are comparable to that of figure 13(b). For example, spectral slope for both the methods can be found to be approximately 0.06 dB MHz^{-1} within the frequency band 10–200 MHz for normal RBC. The computational results for $\theta = \pi/2$ are presented in figures 13(c) and (d) for those methods, respectively. These figures demonstrate good correspondence between the methods for each particle. It was observed that the k-Wave tool box took about 18 min on a personal computer to simulate PA signals from a normal or pathological RBC. The execution time for the same computer evaluating a PA signal for one detector location was less than a minute for the approach presented here. The computational time for the current method would increase if multiple detector positions are considered. However, for the k-Wave method, the simulation time would not change even though signals are measured from many directions. In general, the present method is a faster method than the k-Wave method and is sufficient since in our flow cytometry application only one transducer (and thus detector location) is used.

The results presented in this paper are also cosistent with those of previous publications [19, 20]. The first minimum in the experimental spectrum appeared to be at about 800 MHz for a normal RBC for $\theta = 0°$. However, it occurs at 640 MHz for our case. In this work, we assumed that the acoustic properties (density and speed of sound) of PA source and the surrounding medium were the same. Nevertheless, this was not the case during the experiment. The density and speed of sound for RBC are higher than those of the saline water. The speed of sound inside RBC controls the wave-number of a wave and thus dictates the locations of frequency minima.

In this work, we restricted ourselves to the axisymmetric shapes. These shapes can be represented well with the Legendre polynomial expansion, as shown for RBCs. However, RBC-shapes under the influence of

[6] The spatial grid size was chosen to be 1024 × 1024 with a resolution of 0.2 μm.

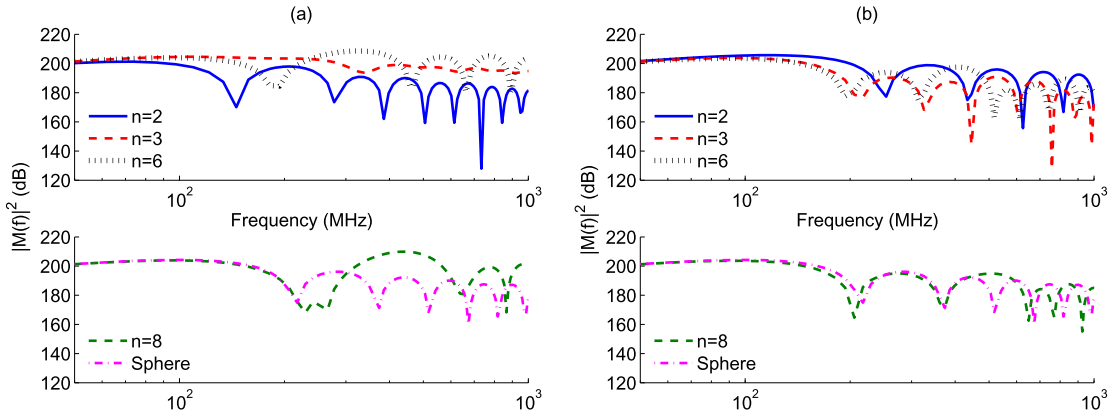

Figure 9. (a) Variations of $|M(f)|^2$ with ultrasonic frequency for the Chebyshev particles ($\epsilon = 0.25$) along $\theta = 0$. (b) Similar to (a) but for $\theta = \frac{\pi}{2}$. Each figure is divided into two parts (upper and lower panels) to improve the clarity of the lines.

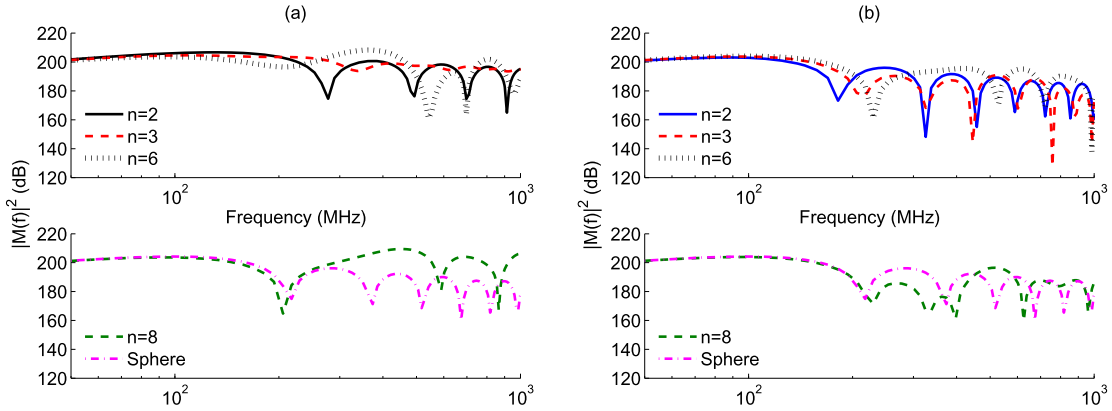

Figure 10. Representative graphs of $|M(f)|^2$ for the Chebyshev particles with $\epsilon = -0.25$ for two perpendicular directions ($\theta = 0$ in (a) and $\theta = \frac{\pi}{2}$ in (b)). For each direction, some of the lines are plotted in the upper panel and rest of the lines are displayed in the lower panel.

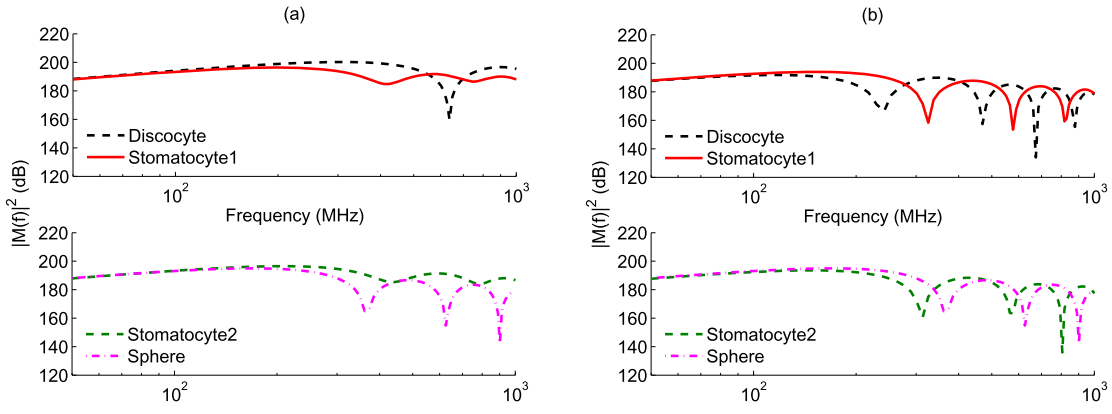

Figure 11. Computed $|M(f)|^2$s for normal and pathological RBCs as a function of frequency. (a) The quantity is evaluated in the $\theta = 0$ direction. It has two parts (upper and lower panels). (b) Same as (a) but for $\theta = \frac{\pi}{2}$.

certain agents become complex and nonaxisymmetric. Such shapes can be fitted well using the spherical harmonic expansion facilitating parameterization of surfaces. This is known as parametric surface modeling. The parametric surface modeling is an active research area in medical image analysis [29, 30]. Therefore, complex nonaxisymmetric shapes (e.g. echinocyte states) could be modeled using the spherical harmonic expansion. Those results could be compared to those of a normal RBC. It might also be speculated that PA images of cells and organelles could be parameterized through the spherical harmonic expansion for

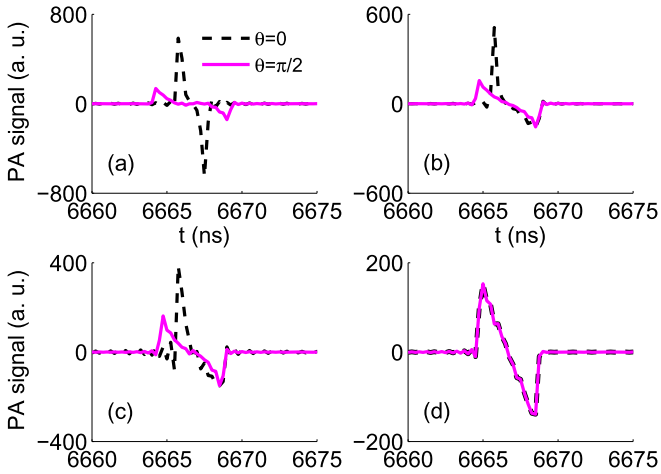

Figure 12. Plots of PA signals generated by normal and pathological RBCs. The signals along ($\theta = 0$) and perpendicular ($\theta = \pi/2$) to the axis of symmetry are shown. (a) Discocyte, (b) Stomatocyte1, (c) Stomatocyte2, (d) Sphere.

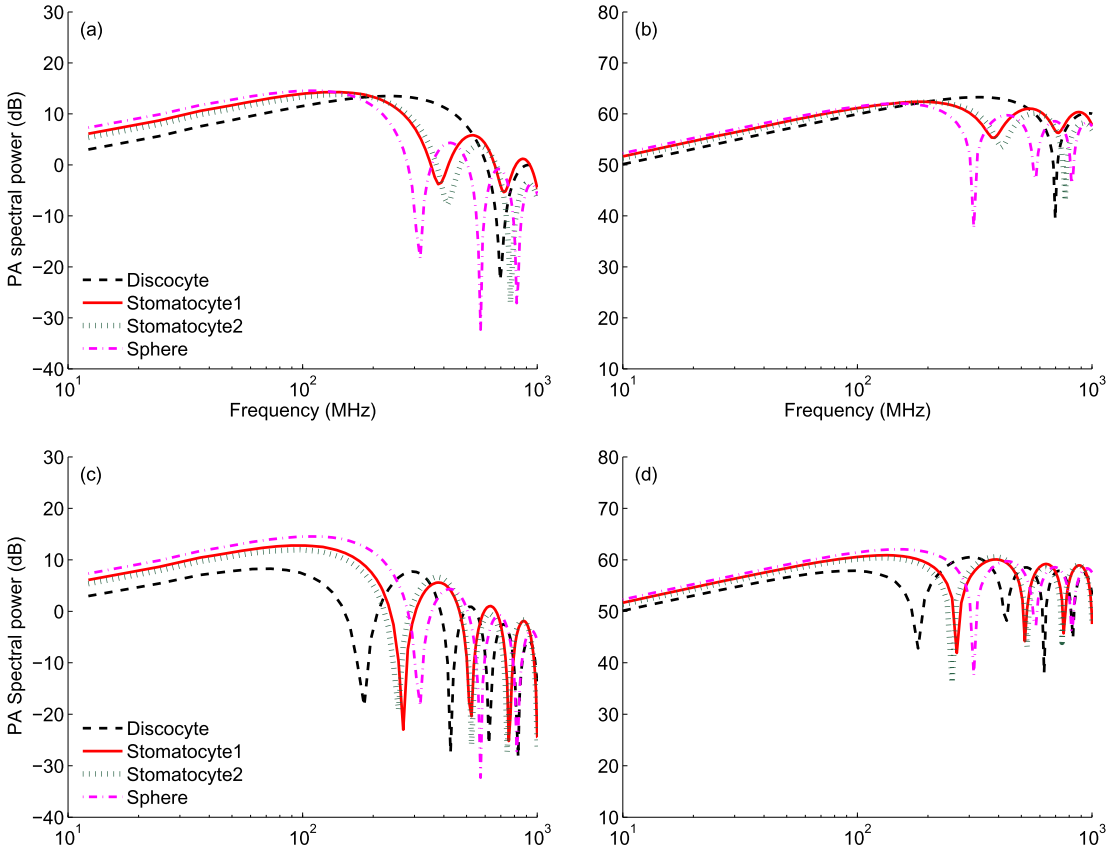

Figure 13. Plots of spectral power for four RBC shapes (i.e. normal RBC, stomatocyte1, stomatocyte2 and equivalent sphere). (a) The spectral lines obtained using the k-Wave tool box $\theta = 0$. (b) The same lines for a Green's function approach. (c) and (d) The same curves by those methods, respectively for $\theta = \pi/2$.

quantitative evaluation of their morphologies. Additionally, the PA technique is a unique modality that can provide spectral information which in turn may help to cross-check the accuracy of parametrization.

The rapid analysis of spectral features is critical for the work on the determination of cell shape and size using the PA methods. Measurements using the PA signal analysis have been used to calculate the nucleus to cytoplasmic ratio of cells for the differentiation of cells [32]. We have recently incorporated such high frequency transducers in microfluidic devices, and are working on differentiating different cell types [33]. In this approach, we need to perform a best fit to the PA data measured for thousands of signals collected from cells. In the long term, we aspire to perform analysis of the PA signals in near real time for the rapid

characterization and classification of cells in our PA/acoustic flow cytometer.

In conclusion, the PA fields in the far field region for nonspherical axisymmetric fluid particles were derived using a Green's function approach. The analytical expression for differential PA cross-section was also presented. The Legendre polynomial expansions were utilized to fit theoretically constructed RBC contours representing discocyte and stomatocytes. The location of the first frequency minimum for the spheroidal droplet decreased as the aspect ratio increased. It varied from 600 to 50 MHz for the particles considered in this study, for the measurement direction $\theta = 0°$. However, for $\theta = 90°$ the location of the first frequency minimum increased with increasing aspect ratio. The same graphs for higher order ($n = 6, 8$) Chebyshev particles exhibited a close match to that of a homogeneous sphere up to first frequency minimum from both observation directions (along and lateral to the axis of symmetry). The PA spectra for normal and pathological RBCs were different. For stomatocyte states, the first minimum occurred (420 MHz) much earlier than that of healthy RBC (640 MHz) when measured from $\theta = 0°$ direction. However, for $\theta = 90°$ minima appeared at about 310 and 240 MHz, respectively. Much insight could be gained from this study as to how locations of frequency minima depend on the width of the PA source along the direction of measurement. Moreover, it might be possible to assess cellular morphology from the PA spectral pattern. Identification of the particle state based on the spectral features detected for frequencies between 100 and 1000 MHz is critical for our current work on the detection of RBC pathology. The approach that relies on simultaneous irradiation of the particles with light and ultrasound, and identification of the particle state based on the spectral features that are derived from the signals measured [19, 20].

Acknowledgments

RKS would like to thank late Prof Binayak Dutta-Roy of Saha Institute of Nuclear Physics, Kolkata for stimulating discussion on fitting of axisymmetric nonspherical shapes with the Legendre polynomial expansion. MCK would like to thank Natural Sciences and Engineering Research Council of Canada/Canadian Institutes of Health Research (Collaborative Health Research Projects grant # 462315-2014) for funding.

References

[1] Spurr R, Wang J, Zeng J and Mishchenko M I 2012 Linearized *T*-matrix and Mie scattering computations *J. Quant. Spectrosc. Radiat. Transfer* **113** 425–39
[2] Waterman P C 1971 Symmetry, unitarity, and geometry in electromagnetic scattering *Phys. Rev.* D **3** 825–39
[3] Bi L and Yang P 2013 Modeling of light scattering by biconcave and deformed red blood cells with the invariant imbedding *T*-matrix method *J. Biomed. Opt.* **18** 055001
[4] Draine B T and Flatau P J 1994 Discrete-dipole approximation for scattering calculations *J. Opt. Soc. Am.* A **11** 1491–9
[5] Lim J, Ding H, Mir M, Zhu R, Tangella K and Popescu G 2011 Born approximation model for light scattering by red blood cells *Biomed. Opt. Express* **2** 2784–91
[6] Faran J J 1951 Sound scattering by solid cylinders and spheres *J. Acoust. Soc. Am.* **23** 405–18
[7] Anderson V C 1950 Sound scattering from a fluid sphere *J. Acoust. Soc. Am.* **22** 426–31
[8] Waterman P C 1969 New formulation of acoustic scattering *J. Acoust. Soc. Am.* **45** 1417–29
[9] Kuo I Y and Shung K K 1994 High frequency ultrasonic backscatter from erythrocyte suspension *IEEE Trans. Biomed. Eng.* **41** 29–34
[10] Sharma S K and Saha R K 2004 On the validity of some new acoustic scattering approximations *Waves Random Media* **14** 525–37
[11] Diebold G J, Sun T and Khan M I 1991 Photoacoustic monopole radiation in one, two and three dimensions *Phys. Rev. Lett.* **67** 3384–7
[12] Saha R K and Kolios M C 2011 A simulation study on photoacoustic signals from red blood cells *J. Acoust. Soc. Am.* **129** 2935–43
[13] Saha R K and Kolios M C 2011 Effects of erythrocyte oxygenation on optoacoustic signals *J. Biomed. Opt.* **16** 115003
[14] Hysi E, Saha R K and Kolios M C 2012 Photoacoustic ultrasound spectroscopy for red blood cell aggregation and oxygenation *J. Biomed. Opt.* **17** 125006
[15] Saha R K, Karmakar S and Roy M 2012 Computational investigation on the photoacoustics of malaria infected red blood cells *PLoS One* **7** e51774
[16] Saha R K 2014 Computational modeling of photoacoustic signals from mixtures of melanoma and red blood cells *J. Acoust. Soc. Am.* **136** 2039–49
[17] Bok T-H, Hysi E and Kolios M C 2016 Simultaneous assessment of red blood cell aggregation and oxygen saturation under pulsatile flow using high-frequency photoacoustics *Biomed. Opt. Express* **7** 2769–80
[18] Saha R K 2015 A simulation study on the quantitative assessment of tissue microstructure with photoacoustics *IEEE Trans. Ultrason. Ferroelectr. Freq. Control* **62** 881–95
[19] Strohm E M, Berndl E S L and Kolios M C 2013 Probing red blood cell morphology using high frequency photoacoustics *Biophys. J.* **105** 59–67
[20] Strohm E M, Berndl E S L and Kolios M C 2013 High frequency label-free photoacoustic microscopy of single cells *Photoacoustics* **1** 49–53
[21] Li Y and Fang H 2013 Photoacoustic pulse wave forming along the rotation axis of an ellipsoid droplet: a geometric calculation study *Appl. Opt.* **52** 8258–69
[22] Li Y, Fang H, Min C and Yuan X 2014 Analytic theory of photoacoustic wave generation from a spheroidal droplet *Opt. Express* **22** 19953–69
[23] Treeby B E and Cox B T 2010 k-Wave: MATLAB toolbox for the simulation and reconstruction of photoacoustic wave fields *J. Biomed. Opt.* **15** 021314
[24] Verawaty and Pramanik M 2016 Simulating photoacoustic waves from individual nanoparticle of various shapes using *k*-Wave *Biomed. Phys. Eng. Express* **2** 035013
[25] Morse P M and Ingard K U 1968 *Theoretical Acoustics* (New York: McGraw-Hill) ch 7, pp 306–99
[26] Mugnai A and Wiscombe W J 1986 Scattering from nonspherical Chebyshev particles: I. Coss sections, single-scattering albedo, asymmetry factor, and backscattered fraction *Appl. Opt.* **25** 1235–44
[27] Lim H W G, Wortis M and Mukhopadhyay R 2002 Stomatocyte-discocyte-echinocyte sequence of the human red blood cell: evidence for the bilayer-couple hypothesis from membrane mechanics *Proc. Natl Acad. Sci.* **99** 16766–9

[28] Reinhart W H and Chien S 1986 Red cell rheology in stomatocyte-echinocyte trasnformation roles of cell geometry and cell shape *Blood* **67** 1110–8
[29] Khairy K and Howard J 2008 Spherical harmonics-based parametric deconvolution of 3D surface images using bending energy minimization *Med. Image Anal.* **12** 217–27
[30] Khairy K, Foo J and Howard J 2010 Shapes of red blood cells: comparison of 3D confocal images with the bilayer-couple model *Cell Mol. Bioeng.* **1** 173–81
[31] Evans E and Fung Y C 1972 Improved measurements of the Erythrocyte geometry *Microvasc. Res.* **4** 335–47
[32] Moore M J, Strohm E M and Kolios M C 2016 Assessment of the nucleus-to-cytoplasmic ratio in MCF-7 cells using ultra-high frequency ultrasound and photoacoustics *Int. J. Thermophys.* **37** 118
[33] Strohm E M, Gnyawali V, De Vondervoort M V, Daghighi Y, Tsai S S H and Kolios M C 2016 Classification of biological cells using a sound wave based flow cytometer *Proc. SPIE 9708, Photons Plus Ultrasound: Imaging and Sensing 2016* p 97081A